JACS
JOURNAL OF THE AMERICAN CHEMICAL SOCIETY

ARTICLE

pubs.acs.org/JACS

Spectroscopic and Computational Studies of α-Keto Acid Binding to Dke1: Understanding the Role of the Facial Triad and the Reactivity of β-Diketones

Adrienne R. Diebold,[†] Grit D. Straganz,*[,§] and Edward I. Solomon*[,†,‡]

[†]Department of Chemistry, Stanford University, Stanford, California 94305, United States

[‡]Stanford Synchrotron Radiation Lightsource, SLAC, Stanford, California 94309, United States

[§]Institute for Biotechnology and Biochemical Engineering, Graz University of Technology, Petersgasse 12, A-8010 Graz, Austria

Supporting Information

ABSTRACT:

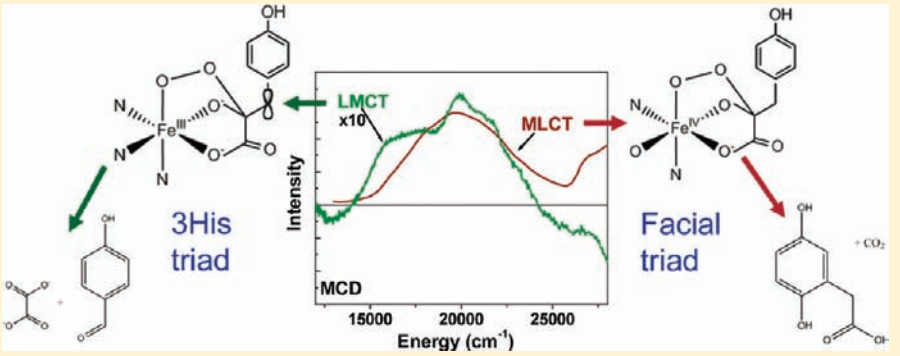

The O_2 activating mononuclear nonheme iron enzymes generally have a common facial triad (two histidine and one carboxylate (Asp or Glu) residue) ligating Fe^{II} at the active site. Exceptions to this motif have recently been identified in nonheme enzymes, including a 3His triad in the diketone cleaving dioxygenase Dke1. This enzyme is used to explore the role of the facial triad in directing reactivity. A combination of spectroscopic studies (UV−vis absorption, MCD, and resonance Raman) and DFT calculations is used to define the nature of the binding of the α-keto acid, 4-hydroxyphenlpyruvate (HPP), to the active site in Dke1 and the origin of the atypical cleavage (C2−C3 instead of C1−C2) pattern exhibited by this enzyme in the reaction of α-keto acids with dioxygen. The reduced charge of the 3His triad induces α-keto acid binding as the enolate dianion, rather than the keto monoanion, found for α-keto acid binding to the 2His/1 carboxylate facial triad enzymes. The mechanistic insight from the reactivity of Dke1 with the α-keto acid substrate is then extended to understand the reaction mechanism of this enzyme with its native substrate, acac. This study defines a key role for the 2His/1 carboxylate facial triad in α-keto acid-dependent mononuclear nonheme iron enzymes in stabilizing the bound α-keto acid as a monoanion for its decarboxylation to provide the two additional electrons required for O_2 activation.

1. INTRODUCTION

The mononuclear nonheme iron enzymes are an important group with a diverse range of medical and pharmaceutical applications. This class is divided into oxygen and substrate activating enzymes depending on the route taken to overcome the spin forbidden reaction of organic substrates with O_2. One of the major categories of O_2 activating enzymes is the α-keto acid-dependent dioxygenases.[1−5] These enzymes use an α-keto acid cofactor to provide electrons for the reduction of dioxygen. Reaction with dioxygen leads to decarboxylation of the α-keto acid and formation of a reactive Fe^{IV}=O species, which is competent for a number of different reactions including hydroxylation, H-atom abstraction, desaturation, and halogenation.[1−3] Among the O_2 activating enzymes, a conserved "facial triad" motif of two histidine residues and one carboxylate (Asp or Glu) tethers Fe^{II} to the protein on one face of an octahedron. This facial triad (as it will be referred to in the remainder of this work) is generally found to be functionally important for the oxygen activating subclass.[5] Recently, a number of enzymes with perturbations to the facial triad have been defined. The α-keto acid-dependent halogenases CytC3 and SyrB2 lack the carboxylate of the facial triad, and a halogen anion is coordinated in its place.[6,7] In cysteine dioxygenase and the β-diketone cleaving dioxygenase Dke1, the carboxylate is replaced by a histidine residue to form a 3His triad.[8,9]

Received: April 1, 2011
Published: August 26, 2011

dx.doi.org/10.1021/ja203005j | J. Am. Chem. Soc. 2011, 133, 15979–15991

In the native enzyme reaction, Dke1, from *Acinetobacter johnsonii*, cleaves acetylacetone (acac) with incorporation of both atoms of dioxygen to form methyl glyoxal and acetate (Scheme 1).[9] Previous work on Dke1 showed that the ligand field at the resting ferrous site was not significantly affected by the change from a facial triad to a 3His triad.[10,11] Upon acac binding, the strong donation of the acac ligand drives the loss of a H_2O ligand leading to an open coordination position on the Fe^{II} for the O_2 reaction[11] (similar to the general mechanistic strategy observed for many of the facial triad enzymes[1]). From ref 11, two key experimental results suggested that an important difference between the facial and 3His triads is the net difference in charge at the sites. (The Fe^{II}-facial triad has a +1 charge, while the Fe^{II}-3His triad has a +2 charge.[12]) First, the resting ferrous site of Dke1 was found to have a depressed pK_a for water bound at the active site.[10] Additionally, the major spectroscopic difference between the acac-bound ferrous complexes of Dke1 and 4-hydroxyphenlpyruvate dioxygenase (HPPD, a facial triad containing enzyme) was an energy shift in the metal to ligand charge transfer transitions.[11] Both were ascribed to the charge difference at the active site. Recently, an atypical cleavage of the α-keto acid, 4-hydroxyphenylpyruvate (HPP), was reported to be catalyzed by Dke1. Product analysis revealed the *p*-hydroxybenzaldehyde product instead of the homogentisate product found for HPP with HPPD (Scheme 2).[13] This new C2−C3 cleavage is unprecedented for α-keto acid reactions with mononuclear nonheme iron enzymes.

In this study, we use a combination of spectroscopies to define the bonding of the α-keto acid, HPP, to ferrous Dke1. The geometric and electronic structure determined for this site is then used to evaluate the atypical reaction coordinate of the 3His relative to the facial triad. The mechanistic insight from this reaction is then extended to the native reaction of Dke1 with acac. This study defines an important role of the charge of the facial triad in stabilizing the correct bound keto-form of α-keto acid for decarboxylation resulting in two electron transfer to O_2.

2. MATERIALS AND METHODS

2.1. Sample Preparation for Spectroscopy. Dke1 was expressed and purified as described previously.[9,14] Apo-Dke1 was exchanged into deuterated buffer (100 mM Tris−HCl) at pD 7.0 using an Ultrafree-4 filter with a 10 kDa cutoff membrane (Millipore) to a concentration of 2−4 mM. Sucrose was partially deuterated by dissolving in D_2O (1:10 w/v) and incubated overnight allowing for proton/deuteron exchange, then lyophilized to remove excess water. All other reagents were used as received without further purification. Buffer, 4-hydroxyphenylpyruvate (HPP), ferrous ammonium sulfate, and sucrose were made anaerobic by purging with Ar on a Schlenk line. Dke1 was made anaerobic by alternating cycles of vacuum and purging with Ar at 273 K. All samples were prepared in an inert atmosphere, N_2-purged "wet box" to maintain an O_2-free environment. Ferrous ammonium sulfate was dissolved in buffer and added to Dke1 in microliter quantities to a concentration of 90% of the enzyme (monomer) concentration to avoid free iron in the sample. In the "wet box", HPP was partially dissolved in buffer, and then 10 M sodium hydroxide was titrated in dropwise until all solid was dissolved. HPP was added in microliter quantities to a concentration of 5−10 times the concentration of Fe. Sucrose (175% w/v) was added to the sample as a glassing agent for MCD measurements, giving a final sample concentration of 1−2 mM.

2.2. Spectroscopic Methods. NIR (600−2000 nm) MCD spectra were recorded on a Jasco J730 spectropolarimeter with a liquid N_2-cooled InSb detector (Teledyne Judson Technologies) and an Oxford Instruments SM-4000-7T superconducting magnet. UV−vis (300−900 nm) MCD spectra were recorded on a Jasco J810D spectropolarimeter equipped with an extended S20 photomultiplier tube and a SM-4000-7T superconducting magnet. UV−vis absorption spectra were recorded on an Agilent 8453 diode array spectrometer. UV−vis absorption spectra were taken at 278 K in an anaerobic cuvette and were corrected for buffer and protein baseline effects. Natural CD features and baseline effects were eliminated from the MCD spectra by taking the average of the magnitudes of the positive and negative field data. For VTVH MCD, a calibrated Cernox resistor (Lakeshore Cryogenics, calibrated 1.5−300 K), inserted into the sample cell, was used for accurate temperature measurement. The VTVH MCD data obtained were normalized to the intensity maximum, and ground-state parameters were obtained using previously published procedures.[15,16]

Samples for resonance Raman (rR) experiments were prepared anaerobically as described above and run in an anaerobic NMR tube spinning at 298 K. To obtain the O_2 exposed spectra, the NMR tubes were exposed to air for 4 h, and the spectra were retaken. For the ^{18}O exchanged samples, the protein was concentrated in buffer made with $H_2{}^{18}O$ to a final ratio of 80% $H_2{}^{18}O$/20% H_2O. The HPP substrate was dissolved in $H_2{}^{18}O$. The ratio of ^{18}O to ^{16}O incorporated into HPP at one position was 2:1 as determined by time of flight mass spectroscopy. The rR spectra were recorded on an Andor Newton charge coupled device (CCD) detector cooled to −80 °C with a triple monochromator (Spex 1877 CP with 1200, 1800, and 2400 grooves/mm holographic spectrograph gratings). Excitation at 363.8 nm was provided by an Ar^+ (Innova Sabre 25/7) ion laser with incident power in the 40−80 mW range using an ~135° backscattering configuration. Background spectra of charcoal in NMR tubes were used for baseline subtraction.

Scheme 1. Native Reaction Catalyzed by Dke1

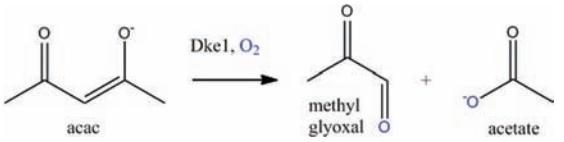

Scheme 2. Dioxygen-Dependent Cleavage of HPP Catalyzed by Dke1 or the Facial Triad

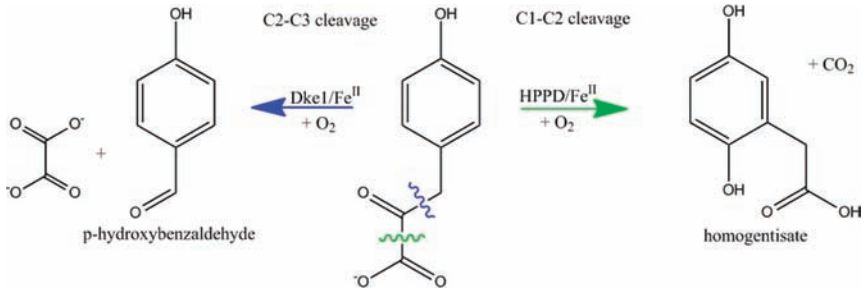

2.3. Computational Methods. The Dke1 active site was modeled using the crystal structure (PDB entry: 3bal) as a starting point. The δ-coordination of one of the histidine residues observed in the crystal structure was preserved. Histidine residues were truncated to methyl imidazole for the model, and constraints imposed by the protein backbone were simulated by fixing the relative positions of the β-carbons of the backbone. The coordination of the active site was completed with either a keto (monoanion) or enolate (dianion) bidentate coordinated HPP ligand or a monoanionic acac ligand.

Density functional theory (DFT) calculations were performed using Gaussian 03[17,18] with the spin unrestricted functional BP86[19] with 10% Hartree−Fock exchange[20] and under tight convergence criteria. For the ferrous ES complexes, the triple-ζ basis set 6-311G* was used to describe Fe and the OC−CO_2 moiety of HPP; the double-ζ basis set 6-31G* was used to describe all other atoms. For the reactivity studies, the triple-ζ basis set was extended to include O_2, C3 for HPP(enolate) and the O−C−C−C−O moiety of acac. The stationary structures were optimized and found to be stable with no imaginary frequencies > −25 cm^{-1} (which were associated with the constraints placed on the β-carbons). Cartesian coordinates for all stationary points are given in the Supporting Information. Transition state structures were determined using the QST2 transition search function in G03 and were found to have one imaginary frequency, which correlated to the motion of the bond being broken or formed. Solvation effects were included by applying the polarized continuum model (PCM)[21] with a dielectric constant $\varepsilon = 4.0$. The energies given include thermal and zero-point corrections. Structures were visualized with GaussView 3.09;[22] orbital compositions were determined with QMForge;[23] and molecular orbitals were visualized with Molden version 4.1.[24] Time-dependent DFT (TD-DFT) calculations were performed to compare to the experimental spectra, and SWizard was used to parse the results.[25,26]

3. RESULTS

3.1. Spectroscopic. NIR MCD spectroscopy of Fe^{II} sites probes the energy splitting of the five d orbitals by the ligand environment. In an octahedral, 6-coordinate, 6C, site, the d orbitals split into a ground t_{2g} and excited e_g set separated by ~10 000 cm^{-1} for nonheme ligands. The e_g set is further split in energy by the low symmetry protein environment. 6C Fe^{II} sites exhibit two transitions in the 10 000 cm^{-1} region split by ~2000 cm^{-1}. For 5C, the splitting is larger leading to transitions in the ~10 000 and 5000 cm^{-1} region. For 4C sites, the ligand field (LF) is weak (10 Dq_{Td} = −4/9 10Dq_{Oh}), leading to transitions in the 5000−7000 cm^{-1} region. For the high spin d^6 center in octahedral symmetry, the extra electron in the t_{2g} orbitals gives a $^5T_{2g}$ ground state. This is also split in energy due to the low symmetry of the protein environment combined with in state spin−orbit coupling (SOC). This leads to a non-Kramers doublet ground state defined by its zero field splitting (ZFS) parameters δ and $g_{||}$.[1] These can be obtained from VTVH MCD data and related to the splitting of the t_{2g} set of d orbitals (Δ, the axial splitting, and V, the rhombic splitting) as described in ref 16.

3.1.1. NIR VTVH MCD of Dke1−HPP. The 5 K, 7 T MCD spectrum of resting (Fe^{II}-bound) Dke1 has been published previously. It shows two transitions at 9100 and 10 900 cm^{-1} indicating a 6C site.[11] Addition of 10 equiv of HPP to resting Dke1 results in the 5 K, 7 T MCD spectrum shown in Figure 1 (green). Two transitions are observed in this spectrum: a broad transition at ~9500 cm^{-1} and the low energy tail of a transition (peaking at less than 5500 cm^{-1}). The VTVH MCD isotherms were taken at 9400 cm^{-1} (arrow in Figure 1, green) and are shown in the inset to Figure 1 with the best fit to the data. The

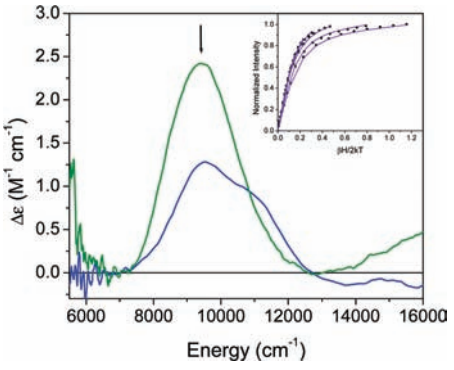

Figure 1. VTVH MCD of Dke1−HPP. The 5 K, 7 T MCD spectrum of Dke1−HPP (green) and resting ferrous (blue, adapted from ref 12). The arrows indicate the energy at which the VTVH MCD isotherms were recorded. Inset: VTVH MCD isotherms taken at 9400 cm^{-1}. The error bars are within the size of the data points.

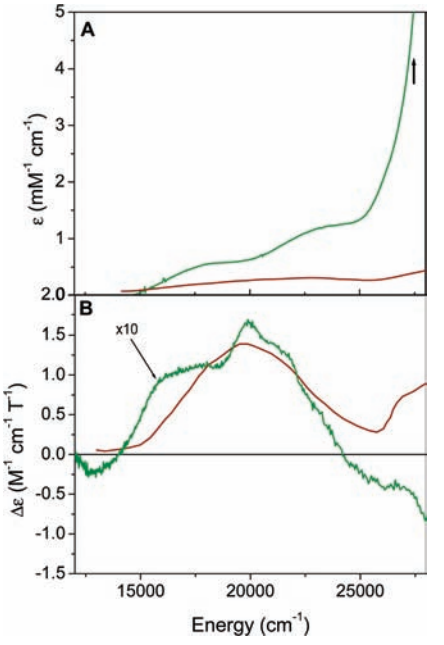

Figure 2. UV−visible absorption and MCD spectra of Dke1−HPP (green). The spectra for HPPD−HPP (red) are included for reference (adapted from refs 27 and 30). (A) 298 K absorption spectra; (B) 5 K, 7 T MCD spectra.

Dke1−HPP VTVH MCD data fit to a negative zero field split system with ground-state splitting parameters of δ = 3.1 ± 0.2 cm^{-1} and $g = 9.0 \pm 0.2$ giving $\Delta = -600 \pm 150$ cm^{-1} and $|V|$ = 260 ± 60 cm^{-1}. In both of the resting Dke1 and Dke1−HPP complexes, there are transitions in the 8500−12 000 cm^{-1} region (Figure 1, green and blue); however, the transition in Dke1−HPP is significantly more intense than the transitions of resting Dke1. This increase in intensity indicates that the transition observed for Dke1−HPP in the 8500−12 000 cm^{-1} region results from the binding of HPP to the Fe^{II} center and is not residual resting Dke1. Additionally, the ground-state parameters from the fit to the VTVH MCD isotherms in Dke1−HPP differ from those of resting Dke1. (VTVH MCD isotherms of resting Dke1 were taken at 8850 cm^{-1} and fit to a negative

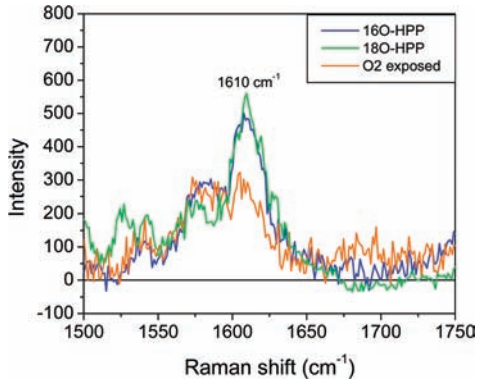

Figure 3. Resonance Raman shift for Dke1−HPP (blue), Dke1−HPP-(^{18}O) (green), and the O_2 exposed control (orange). The spectra were taken at 298 K using an excitation wavelength of 363.8 nm.

zero field split system with ground-state splitting parameters $\Delta = -300 \pm 100$ cm^{-1} and $|V| = 140 \pm 40$ cm^{-1}.) From the energy of the transition and the fit to the VTVH MCD data for Dke1−HPP, the transition at ~9500 cm^{-1} reflects a 6C site with HPP bound. While HPP-bound Dke1 has a transition at <5500 cm^{-1}, there is no equivalent feature present for the resting Dke1 complex (Figure 1, blue in that same energy region). The presence of a low energy (<5500 cm^{-1}) transition reflects a 5C site for HPP-bound Dke1. Taken together, these data indicate that the active site of Dke1−HPP is a mixture of 5C and 6C sites. This 5C/6C mixture was also observed for acac bound to Dke1.[11] The presence of 5C Fe^{II} in Dke1−HPP demonstrates that an open coordination position at the Fe^{II} active site is available for reaction with O_2.

3.1.2. UV−Vis Absorption and MCD of Dke1−HPP. The UV−visible absorption spectrum of Dke1−HPP is shown in Figure 2A (green). It is characterized by transitions at ~17 500 cm^{-1} ($\varepsilon \approx$ 700 M^{-1} cm^{-1}), ~22 500 cm^{-1} ($\varepsilon \approx$ 1400 M^{-1} cm^{-1}), and ~30 000 cm^{-1} ($\varepsilon \approx$ 12 000 M^{-1} cm^{-1}). The transitions in the UV−vis absorption of Dke1−HPP are significantly more intense than those of HPP bound to the facial triad containing enzyme, HPPD (Figure 2A, red), which has an $\varepsilon \approx 350$ M^{-1} cm^{-1} for the ~20 000 cm^{-1} transition.[27]

The UV−vis 5 K, 7 T MCD spectrum of Dke1−HPP (Figure 2B, green) shows only a very weak pair of transitions at ~17 000 and ~21 500 cm^{-1}.[28] This is in stark contrast to the 5 K, 7 T MCD spectrum of HPPD−HPP (Figure 2B, red),[29] which is an order of magnitude more intense than that of Dke1−HPP.

3.1.3. Resonance Raman. Excitation at 363.8 nm (arrow in Figure 2)[30] into the intense charge transfer of Dke1−HPP resulted in a single resonance enhanced band at 1610 cm^{-1} (Figure 3, blue). This feature does not shift upon ^{18}O−isotope substitution into the carbonyl position of HPP (Figure 3, green). Exposure of the Dke1−HPP sample to O_2 as a control resulted in loss of the 1610 cm^{-1} feature to produce the orange spectrum in Figure 3. Previous rR on the α-keto acid-dependent mononuclear nonheme Fe dioxygenase TauD showed a resonance enhanced (excitation into the Fe^{II} to α-ketoglutarate π^* MLCT at 568.2 nm) band at 1686 cm^{-1}, which shifted to 1648 cm^{-1} on ^{18}O-isotope substitution of α-ketoglutarate.[31] Resonance Raman on well-defined Fe^{II}-model complexes with pyruvate have shown a C=O stretch in the range of 1650−1695 cm^{-1}, enabling the assignment of the band at 1686 cm^{-1} in TauD−α-ketogluatarate as a C=O stretch.[31] The energy of the vibration observed in Dke1−HPP is significantly shifted down in energy relative to the C=O stretch observed in TauD−α-ketoglutarate and shows no isotope shift, suggesting a different assignment for this vibration. Assignment of this vibration will be further explored in section 4.1.

Scheme 3. Tautomerization of HPP

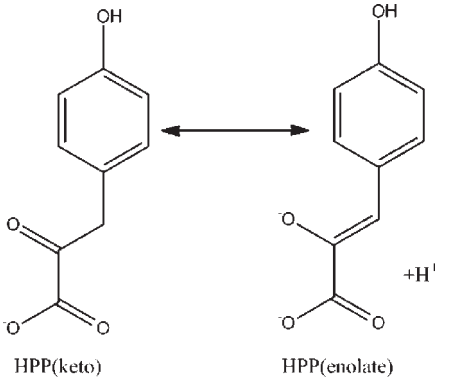

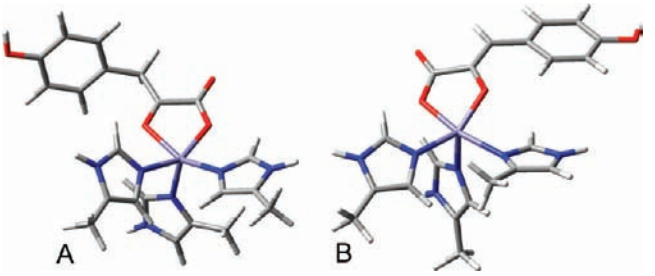

Figure 4. Geometry-optimized structures of (A) Dke1−HPP(keto) and (B) Dke1−HPP(enolate). Key distances and angles given in Table S1.

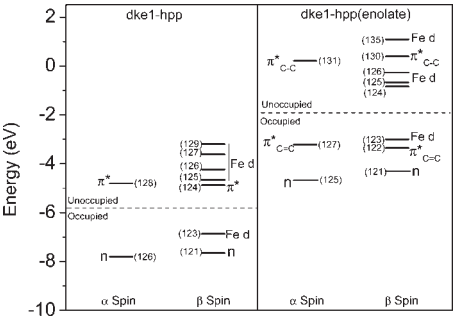

Figure 5. Molecular orbital energy level diagrams for (A) Dke1−HPP-(keto) and (B) Dke1−HPP(enolate).

3.2. Computational. Because of the atypical cleavage pattern for Dke1 with HPP, the increased intensity in the UV−vis absorption spectrum but decreased intensity in the low temperature MCD spectrum (as compared to HPPD−HPP), and the shift in the observed resonance Raman feature (of Dke1−HPP as compared to TauD−α-ketoglutarate), two possible binding modes for the Dke1−HPP complex were explored. The carbonyl moiety of an α-keto acid can tautomerize to form the enol

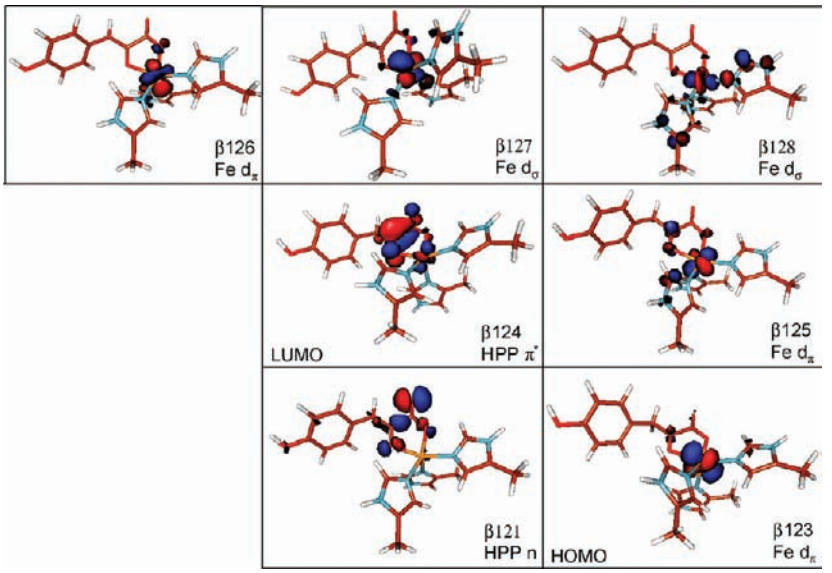

Figure 6. Molecular orbital contours for selected β orbitals of Dke1−HPP(keto).

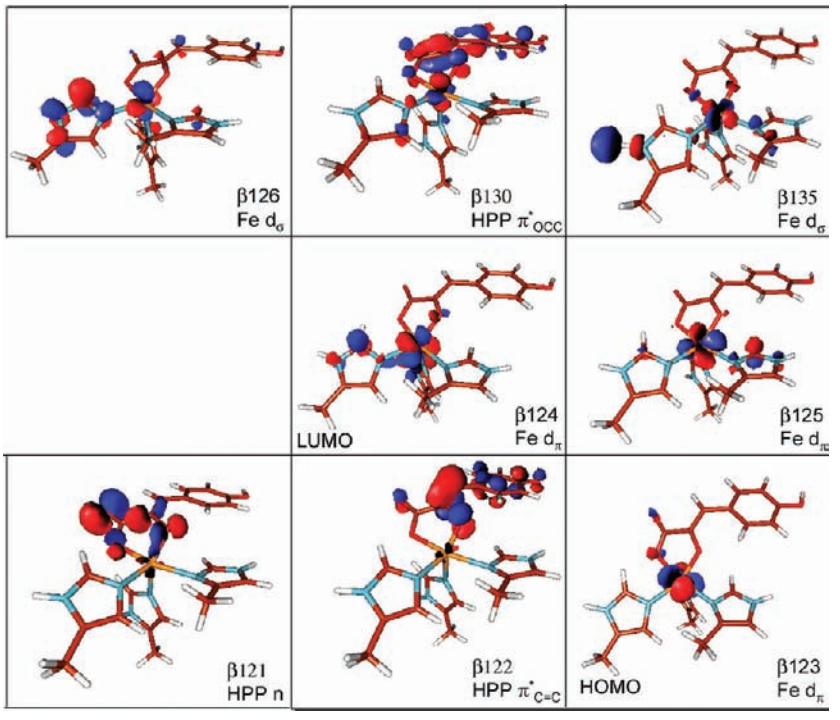

Figure 7. Molecular orbital contours for selected β orbitals of Dke1−HPP(enolate).

(or deprotonated enolate) as in Scheme 3. Previous work on model complexes has shown that monoanionic enolized derivatives of phenylpyruvate will bind to Fe through the same oxygens as the keto form of phenylpyruvate.[32] Thus, both tautomers of HPP were evaluated in the binding of HPP to Dke1.

3.2.1. Geometry-Optimized Structures. The keto and enolate forms of HPP were added to the previously optimized structure of resting Dke1[11] (3His, 3 H_2O ligands) with all three water molecules removed to generate a 5-coordinate Dke1−HPP complex. The geometry-optimized structures of Dke1−HPP-(keto) and Dke1−HPP(enolate) are shown in Figure 4. (Key bond lengths and angles are given in Table S1 of the Supporting Information.) The molecular orbital energy level diagrams for both complexes are shown in Figure 5 with the corresponding contours in Figures 6 and 7 for Dke1−HPP(keto) and Dke1−HPP(enolate), respectively. In both cases, HPP is bound bidentate through one of the carboxylate oxygens, and the oxygen of the carbonyl/alkoxide and the Fe center remains ferrous.[33]

3.2.2. Electronic Structure of Enolized HPP. There are two valence orbitals for the keto and three for the enolate tautomers that are available for bonding to Fe (Figure 5).[34] The valence

dx.doi.org/10.1021/ja203005j |J. Am. Chem. Soc. 2011, 133, 15979–15991

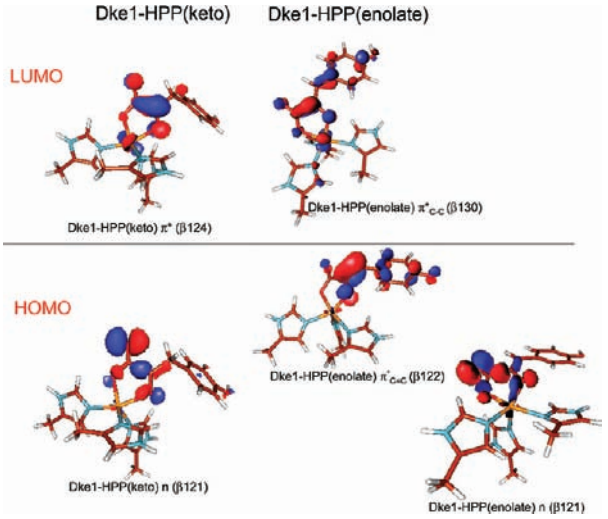

Figure 8. Comparison of valence bonding orbitals available for bonding to Fe^{II} for HPP(keto) and HPP(enolate) in complex with Dke1. (The orbital numbers given are those in Figures 5−7.)

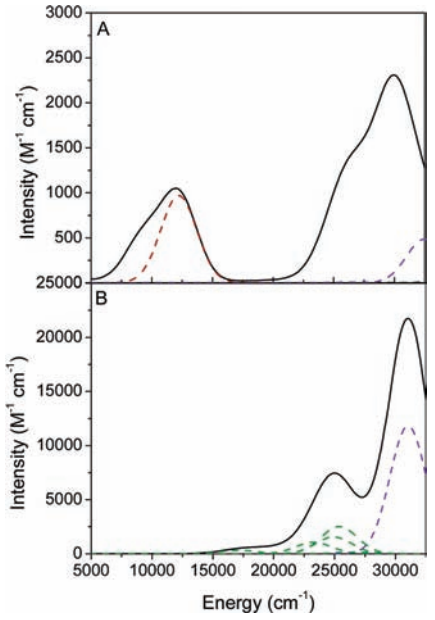

Figure 9. TD-DFT calculated absorption spectra for (A) Dke1−HPP-(keto) and (B) Dke1−HPP(enolate). The transitions (with Gaussian broadening) for MCLT (red), LMCT (green), and intraligand (purple) are shown. Note that the intensity in (A) for the ~20 000−27 500 cm^{-1} region is predicted to have dominantly Fe^{II}−His MLCT transitions (not indicated by Gaussians, but included in the spectral simulation), which has been found before with the 3His model (ref 12).

orbitals of the keto form of α-keto acids have been described previously.[35] They are an occupied α-keto acid n orbital, which is primarily a lone pair on the carboxylate, and the unoccupied α-keto acid π^* orbital, which is concentrated on the carbonyl (Figure 8, left). In the enolate form, the lowest energy valence orbital is an occupied n type orbital with density primarily on the carboxylate (Figure 8, right, bottom). Higher in energy but still occupied, there is a π^* type antibonding (with respect to the alkoxide) orbital with electron density concentrated on the C═C

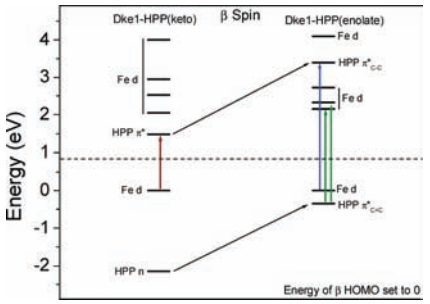

Figure 10. Comparison of MLCT and LMCT in the keto and enolate forms of HPP. The black arrows correlate to the highest occupied and lowest unoccupied orbitals of HPP. The colored arrows correlate to the potential ML (red and blue) or LM (green) CT transitions.

double bond ($\pi^*_{C=C}$, Figure 8, right, middle). Finally, there is an unoccupied π^* antibonding (with respect to the alkoxide) orbital with bonding electron density concentrated on the C−C single bonds (π^*_{C-C}, Figure 8, right, top), similar to the π^* of the keto form, but with additional bonding electron density on the C−C bond adjacent to the phenyl ring.

4. ANALYSIS

4.1. Spectral Assignments. Time-dependent DFT (TD-DFT) calculations were used to evaluate the transitions for both keto and enolate forms of HPP bound to the Dke1 Fe^{II} site. These predicted spectra are plotted in Figure 9 with Gaussian broadening of the transitions predicted to involve Fe^{II}−HPP-(keto) (red), HPP(enolate) (green), and intraligand (purple) transitions. In Figure 9A for the Dke1−HPP(keto) complex, the dominant Fe^{II}−HPP(keto)-based transition (at ~13 000 cm^{-1}, red) is a metal-to-ligand charge transfer (MLCT) transition from the occupied β Fe d_π to the HPP(keto) π^* (123 → 124β in Figure 5, left). An intraligand transition from the HPP(keto) n to π^* orbitals (121 → 124β, 126 → 128α) is predicted at >32 000 cm^{-1} (purple). This description of MLCT and intraligand transitions is the same as has been defined for HPP bound to the Fe^{II} facial triad in HPPD.[27,35] The predicted absorption spectrum for the Dke1−HPP(enolate) complex is very different (Figure 9B) from that of the Dke1−HPP(keto) predicted spectrum. For the enolate bound form, the transitions at 18 000 and ~25 000 cm^{-1} (green) are now ligand-to-metal charge transfer (LMCT) transitions from the HPP(enolate) $\pi^*_{C=C}$ to the unoccupied Fe d_π orbitals (122 → 124,125β in Figure 5, right). The predicted transition at ~31 000 cm^{-1} (Figure 9B, purple) is assigned as the intraligand transition from the $\pi^*_{C=C}$ to the π^*_{C-C} (122 → 130β) in Figure 8, right.

This difference in the nature of the charge transfer transitions (MLCT for keto or LMCT for enolate) leads to a change in the predicted absorption transition intensity. The transitions for Dke1−HPP(enolate) are significantly more intense than the Dke1−HPP(keto) charge transfer (note the intensity scales in Figure 9). The previously studied Fe^{II} model complexes with enolized derivatives of phenylpyruvate also experimentally exhibited a large increase in molar extinction coefficient in their absorption spectra.[32] Alignment of the β manifolds from Figure 5 to the occupied Fe d_π orbital (Figure 10) provides insight into this difference between the predicted transitions. For the Dke1−HPP-(keto) complex (Figure 10, left), the α-keto acid π^* unoccupied orbital is low in energy enabling MLCT (red arrow). Enolization

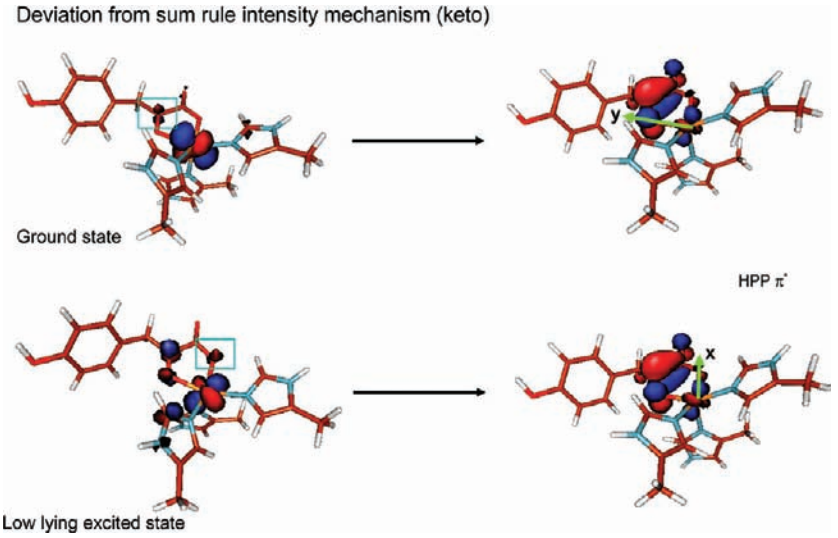

Figure 11. MCD intensity mechanism for the Fe^{II} to HPP(keto) π^* MLCT transition. The ground state and first ligand field excited state MLCT transitions into the HPP(keto) π^* orbital. The two transitions are in perpendicular directions (green arrows show transition moment directions along *y* and *x*, and teal boxes show electron density overlap) and couple through L_z acting on the d_{xz} component of the first excited state (bottom left, which is d_{xy+xz}).

Table 1. C_0/D_0 Ratios for HPPD−HPP and Dke1−HPP

	transition energy	ε (Abs)	$\Delta\varepsilon$ (MCD)	C_0/D_0
HPPD−HPP	20 000 cm^{-1}	350 $M^{-1}\,cm^{-1}$	1.35 $M^{-1}\,cm^{-1}\,T^{-1}$	0.029
Dke1−HPP	17 500 cm^{-1}	700 $M^{-1}\,cm^{-1}$	0.11 $M^{-1}\,cm^{-1}\,T^{-1}$	0.0012
	22 500 cm^{-1}	1400 $M^{-1}\,cm^{-1}$	0.13 $M^{-1}\,cm^{-1}\,T^{-1}$	0.0007

of the HPP ligand shifts the ligand manifold up in energy due to its increased negative charge, which increases the energy of the unoccupied π^*_{C-C} orbital (relative to the occupied Fe d_π; Figure 10, right), which would be an acceptor in the MLCT transition (blue arrow). However, enolization of the HPP ligand also produces the new high energy occupied π^* orbital shown in Figure 8, right middle. This orbital is the donor for LMCT to the unoccupied Fe d_π orbitals (Figure 10, right, green arrows). From the correlation between the assignments of the transitions in the TD-DFT calculations and the experimentally observed absorption spectrum in Figure 2A (an overlay of these two spectra is shown in Supporting Information Figure S1), the charge transfer transitions observed for Dke1−HPP are assigned as LMCT transitions, which arise from an enolized HPP.[36]

Although the experimental absorption intensity of the Dke1−HPP complex is higher than that of HPPD−HPP, the corresponding MCD intensity in Figure 2B is much lower. Estimates of the C_0/D_0 ratios for the transitions in HPPD−HPP and Dke1−HPP are given in Table 1. Previous studies have shown that C_0/D_0 ratios on the order of ~0.01 are typical for charge transfer transitions.[37] The C_0/D_0 ratio of ~0.029 for the MLCT observed for HPPD−HPP is consistent with this, while the C_0/D_0 ratios for the LMCTs observed in Dke1−HPP are an order of magnitude lower (~0.001). Thus, for the LMCT transitions of Dke1−HPP, the MCD intensity is particularly weak.

The MCD intensity mechanism for the MLCT transition in Fe^{II}−α-keto acid complexes has not been previously presented. C-term MCD intensity results from either SOC of two perpendicularly polarized electronic transitions that are close in energy (the pseudo-A mechanism) or a "deviation from sum rule" mechanism in which SOC occurs between the ground state and a low-lying excited state that has a transition to the same excited state that is perpendicularly polarized. For the Fe d to α-keto acid π^* CT transition, a second charge transfer for SOC is lacking; therefore, the intensity is all of one sign (positive, Figure 2B, red) and arises from SOC mixing into the ground state. In this case, the acceptor orbital is the same (HPP(keto) π^* orbital), and the two donor orbitals are different for the ground and low-lying excited states. The transition from the ground state (Figure 11, top) involves excitation of an e^- from the occupied Fe d_π to the HPP(keto) π^* orbital. The low-lying excited state capable of MLCT into this HPP(keto) π^* orbital is the ligand field state involving excitation of the occupied Fe d_π electron into the lowest unoccupied Fe^{II} d_π orbital. The polarization direction of this transition must be perpendicular to that of the MLCT transition from the ground state (which is along the Fe^{II}−HPP-(keto) carbonyl bond). Examination of this transition density in Figure 11, bottom, shows that this is the case (along the Fe^{II}−HPP(keto) carboxylate bond, transition dipole directions indicated by arrows). Finally, these two donor orbitals must SOC in the third mutually perpendicular direction. Defining the open coordination position of the 5C complex as the *z*-axis, the two transitions are *y* and *x* polarized, thus the SOC must involve L_z. In this coordinate system, the occupied Fe d_π β orbital in the ground state is d_{yz} and in the first excited state is primarily d_{xy}, but with some d_{xz} contribution. (Note the tilt of this orbital out of the equatorial plane, Figure 11, bottom right.) The d_{yz} and d_{xz} components will SOC via L_z providing the mechanism for MCD intensity in the MLCT transition observed for the keto form of HPP. Considering the same ground-state mixing mechanism for the LMCT of the enolate, the same ligand donor orbital is involved in both CT transitions, and the low-lying excited state that mixes into the ground state again corresponds to a ligand field excited state involving excitation of the occupied Fe d_π electron into the lowest unoccupied Fe d_π orbital. These transitions are shown in Figure 12. Importantly, in Figure 12, the LMCT transition

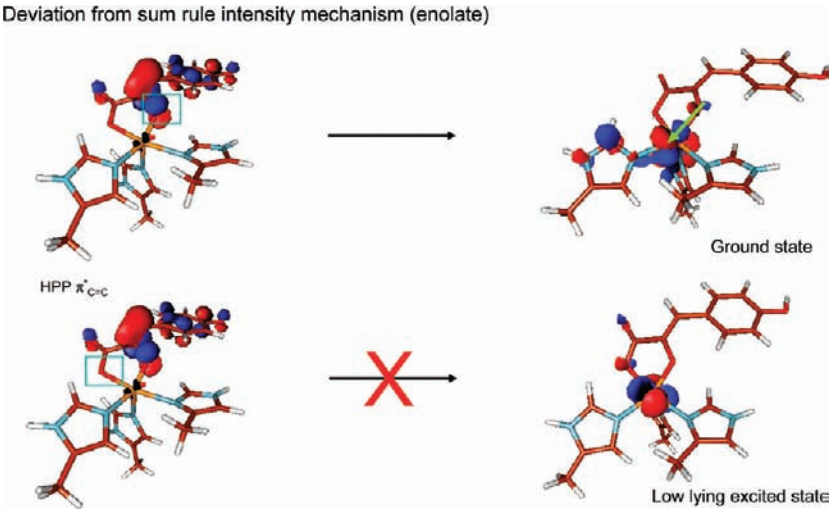

Figure 12. Application of the mechanism for MCD intensity for the Fe^{II} to HPP(keto) π^* MLCT transition to the LMCT transition of Dke1−HPP-(enolate). The ground state and low-lying ligand field first excited state LMCT transitions from the HPP(enolate) π^* orbital. Note (bottom, teal box) there is no electron density overlap of the $\pi^*_{C=C}$ donor orbital and the acceptor orbital for the low-lying ligand field excited state in a direction perpendicular to the polarization direction of the LMCT transition for the ground state ((top) green arrow, polarized along the Fe−O carbonyl bond).

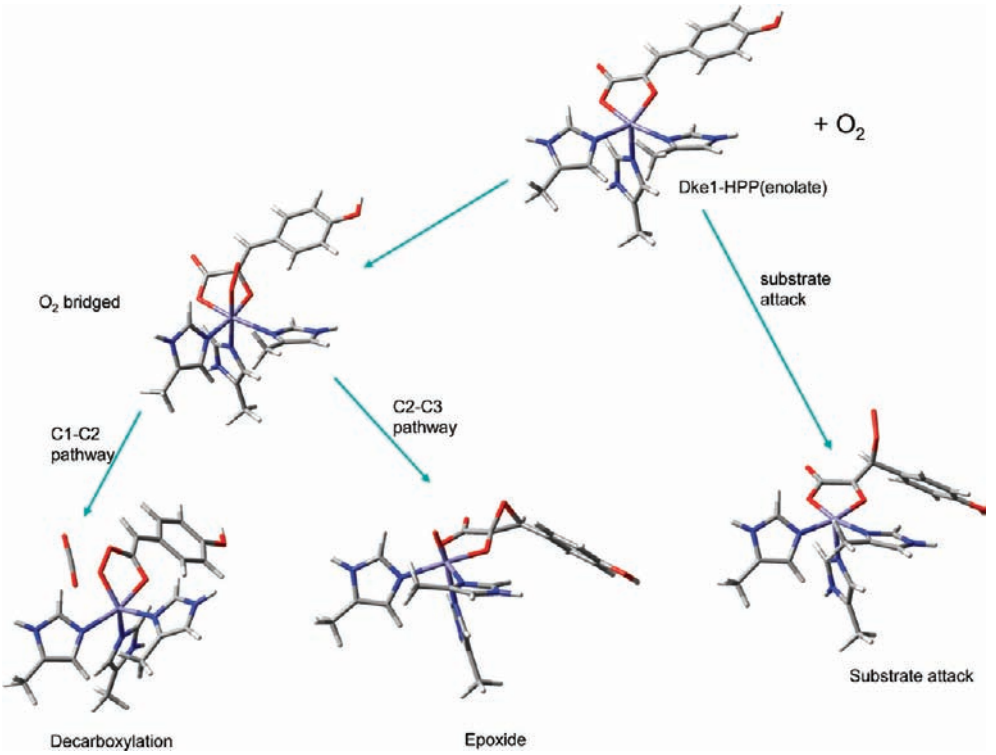

Figure 13. Three potential mechanistic pathways for the O_2 reaction with Dke1−HPP(enolate). O_2 can either react directly with the C═C bond of the enolate (substrate attack, right) or coordinate to Fe and form a bridge to C2 (top left). From the peroxy bridged species, the C−C bond can cleave to release CO_2 (left, C1−C2 pathway), or the O−O bond can cleave to generate an epoxide (middle, C2−C3 pathway). (Structures are geometry optimized and correspond to the equivalently labeled step in Figure 14.)

from the first excited state has no transition density (overlap between the donor and acceptor orbitals) in a direction perpendicular to the ground state (Figure 12, bottom; note lack of orbital character in the teal square of the donor).

As the ground-state intensity mechanism for the MLCT transition in Fe^{II}−α-keto acid is not effective for the LMCT transition in the enolate Fe^{II} complex, we considered the alternative pseudo-A term mechanism in which transitions close in energy SOC. For the Dke1−HPP(enolate) complex, there are LMCT transitions from both the $\pi^*_{C=C}$ and n orbitals to the Fe d_π orbitals that would potentially generate pseudo-A term intensity (Supporting Information, Figure S3). This would be

dx.doi.org/10.1021/ja203005j |J. Am. Chem. Soc. 2011, 133, 15979–15991

consistent with the sign change of the high energy region of the MCD signal in Figure 2B, green. However, from Supporting Information Figure S3, there is little metal d character in the two ligand donor orbitals, and thus little SOC between the transitions. Therefore, this MCD intensity mechanism is also ineffective. In summary, the low intensity in the Dke1−HPP UV−vis MCD spectrum relative to that of HPPD−HPP reflects the difference in the nature of the bonding and associated electronic transitions, MLCT for the keto form of α-keto acid bound to Fe^{II} in HPPD and LMCT for the enolate form of α-keto acid bound to Dke1.

From the assignment of HPP coordinated to Dke1 as an enolate, the 1610 cm^{-1} feature in the rR spectrum in Figure 3 can now be assigned. Enolization of HPP converts the carbonyl to an alkoxide and adds a C=C bond (Scheme 3). Thus, the C=O stretch observed in the 1650−1695 cm^{-1} range for α-keto acids should not be observed for Dke1−HPP. This is confirmed by the DFT calculated vibrational modes for the Dke1−HPP(enolate) complex, which lack any $C_{alkoxide}$−O motion in the 1500−1700 cm^{-1} range. From these calculations, however, the C=C stretch is predicted at 1622 cm^{-1}.[38] Thus, the 1610 cm^{-1} feature in the rR is assigned as the enolate C=C stretch.

4.2. Reaction Coordinate − Dke1−HPP(enolate). Three pathways were evaluated for the reaction of O_2 with the enolized HPP bound to Fe^{II} in the 3His triad (Figure 13): (i) a direct O_2 attack on the substrate (substrate attack); (ii) O_2 activation by the Fe^{II} followed by decarboxylation (the C1−C2 pathway); and (iii) O_2 activation by the Fe^{II} followed by O−O bond cleavage (the C2−C3 pathway).

In the study of Fe^{II}-model complexes with enolized phenylpyruvate derivatives, a mechanism for the reaction with dioxygen was proposed in which the O_2 directly attacks the C3 of the enol double bond.[32] The dioxygen interaction at C3 of the enolate C=C bond of the Dke1−HPP(enolate) complex (direct substrate attack, Figure 13, right) is dissociative on the $S = 3$ surface and has a barrier of ~30 kcal/mol to form bonds on the $S = 1$ and $S = 2$ surfaces[39] (Figure 14, "substrate attack"). This barrier is prohibitive for reaction, ruling out the direct substrate attack mechanism as a potential pathway.

An alternative to the direct attack of dioxygen on the substrate is O_2 coordination to the Fe^{II} center, utilizing the open coordination position at the Fe^{II} site that is observed experimentally (i.e., the low energy d−d transition in Figure 1). Dioxygen binding to the Dke1−HPP(enolate) is approximately thermoneutral in either the $S = 1$ or the $S = 2$ spin states (Figure 14, "O_2 bridged"). Attack on the C2[40] carbon gives a peroxy bridged structure (Figure 13, top left and Figure 14, "O_2 bridged") that is best described as an Fe^{III}−$HPP^{\bullet}$−O_2^{2-} (energy level diagram given for $S = 2$ in Supporting Information Figure S4; the $S = 1$ electronic structure is similar, but with a low spin Fe^{III}). From this structure, either the C−C bond would cleave (Figure 13, bottom left) releasing CO_2 and generating an Fe^{II}−peracid (as occurs in the facial triad sites with α-keto acid) or the O−O bond would cleave to form an Fe^{IV}−epoxide (Figure 13, bottom middle, and Supporting Information Figure S5). Comparison of the energy barriers for decarboxylation and epoxide formation (Figure 14, TS2, orange for decarboxylation vs blue ($S = 1$) and black ($S = 2$) for epoxide formation) shows that the O−O cleavage to form the epoxide is more favorable than decarboxylation by 6−13 kcal/mol. Thus, the most energetically favorable pathway involves interaction of O_2 with the open coordination position at the Fe site to form a bridged-peroxy species. This undergoes O−O bond cleavage to form an Fe^{IV}=O−epoxide complex (Scheme 4). This reaction can occur on either the $S = 1$ or the $S = 2$ spin surfaces with the $S = 1$ slightly lower in energy (Figure 14). In the remaining steps of the reaction, the epoxide could open to form an ester−Fe^{III}−oxo structure with a radical on C3 (Figure 14 "ester" and Supporting Information Figure S4−5). This has an energy barrier of 10 kcal/mol. Oxo attack on C2 would then break the ester bond with a minimal barrier to form the products, *p*-hydroxybenzaldehyde and oxalate, with transfer of one electron back to Fe to regenerate the ferrous site (Figure 14 and Scheme 4).

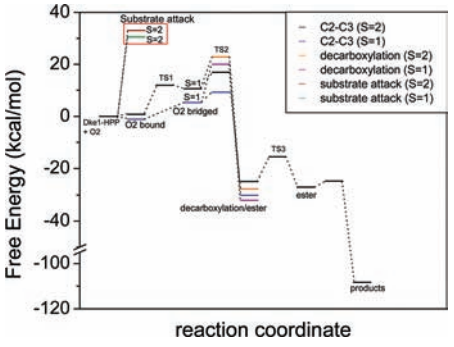

Figure 14. Reaction coordinates for the O_2-dependent cleavage of HPP(enolate) along three pathways: (i) direct substrate attack (red and green); peroxy bridge between Fe and C2 resulting in (ii) decarboxylation (C1−C2 cleavage, orange ($S = 2$) and purple ($S = 1$)); or (iii) C2−C3 cleavage (black ($S = 2$) or blue ($S = 1$)).

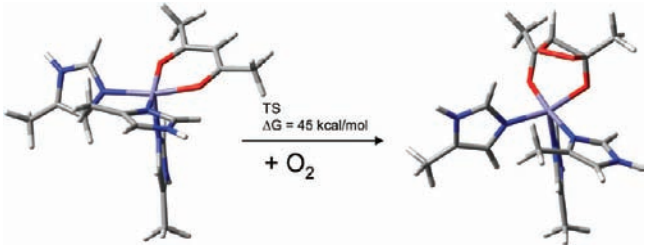

Figure 15. Direct attack of O_2 on acac. Starting 5C acac-bound structure and first O_2 intermediate step. The transition state is shown in Supporting Information Figure S6.

Scheme 4. Metal-Mediated O−O Cleavage in Dke1−HPP

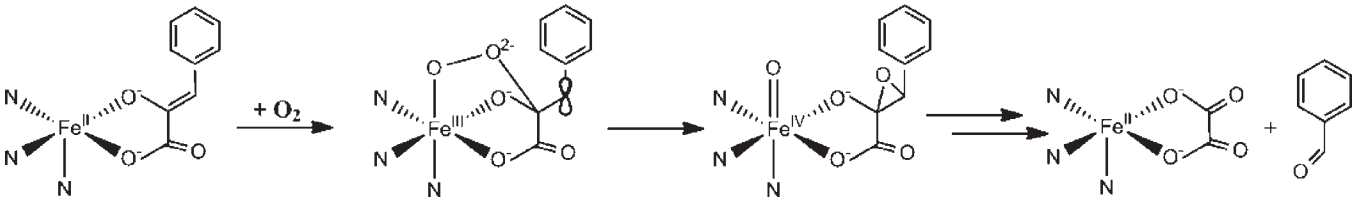

dx.doi.org/10.1021/ja203005j |J. Am. Chem. Soc. 2011, 133, 15979–15991

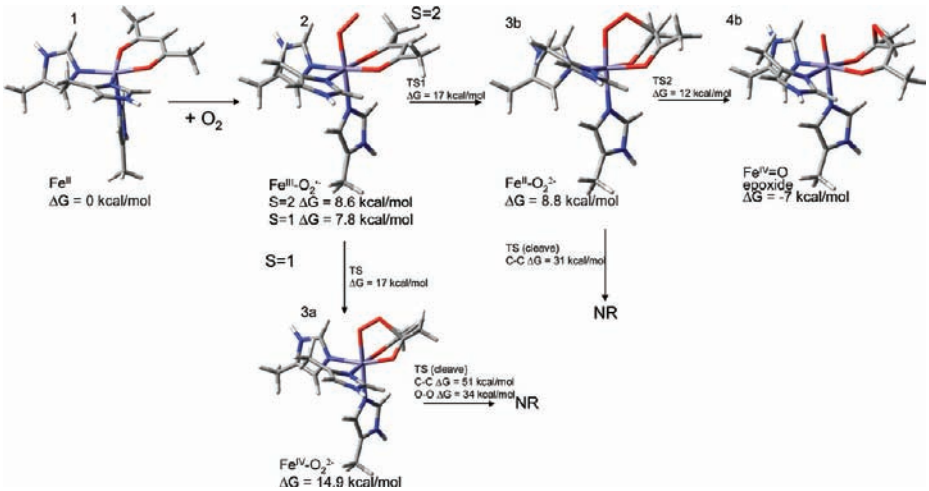

Figure 16. Initial steps for O_2 reaction at Fe for Fe^{II}—acac—O_2. All energies given are relative to 1. O_2 binds to the 5C Fe^{II} site to give 2. Attack at the C2 at C3 carbons in the $S = 1$ and $S = 2$ spin states was evaluated. Formation of a peroxy bridge to C2 in the $S = 1$ spin state (structure 3a) was more favorable than in $S = 2$, and formation of the peroxy bridge to C3 in the $S = 2$ spin state (structure 3b) was more favorable than in $S = 1$. Continuing along the C2 pathway, cleavage of C—C or O—O is energetically inaccessible. Along the C3 pathway, the O—O bond is cleaved with minimal barrier, generating structure 4b, an Fe^{IV}—oxo—epoxide. Cleavage of the C—C bond is energetically less favorable.

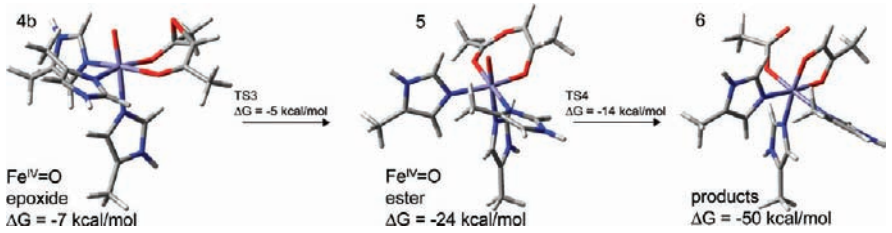

Figure 17. Completion of the Dke1—acac—O_2 reaction on the $S = 2$ surface. The epoxide opens and the oxo attacks the resultant C═C double bond adjacent to the now inserted oxygen to form the experimentally observed products, acetate and methyl glyoxal. Energies given are relative to 1 in Figure 16.

4.3. Reaction Coordinate — Extension to the Native Dke1 Reaction. For the native reaction catalyzed by Dke1, the dioxygenation of the acac substrate to form acetate and methyl glyoxal (Scheme 1), two pathways were considered: (1) the direct attack on the bound substrate by dioxygen, which had been initially proposed,[41] and (2) an Fe-mediated mechanism in which dioxygen binds to the metal to facilitate O_2 attack. The 5C Fe^{II} Dke1—acac complex was taken from the previously published calculation.[11] For the substrate attack, reaction of O_2 with the C3 of acac on the $S = 3$ surface is dissociative. The reaction between O_2 and acac (Figure 15) on the $S = 1$ and $S = 2$ surfaces shows a barrier of ~45 kcal/mol, which is too large for this direct reaction to be relevant in the enzyme. The origin of this barrier (and the associated high barrier for substrate attack in HPP(enolate)) will be considered in the Discussion.

The binding of acac to the ferrous center in Dke1, however, allows the formation of an open coordination position at the Fe^{II} site at which O_2 can react. The strong donor interaction of the acac ligand lowers the energy of the endergonic reaction of O_2 with the Fe^{II} to 8 kcal/mol (for the 3His triad without acac, this is ~20 kcal/mol) resulting in one electron transfer to form an Fe^{III}—$O_2^{\bullet-}$ species (Figure 16, structure 2). From this point, the superoxide can either electrophilically attack the acac HOMO and form a bridge to the C3 carbon or nucleophilically attack the acac LUMO to form a bridge to the C2 carbon. Attack on the C2 carbon occurs on the $S = 1$ surface with the transfer of the second electron from Fe to form an Fe^{IV}—peroxy bridged species (Figure 16, structure 3a). From this peroxy bridged species, the next step, which would be to cleave either the peroxide or the adjacent C—C bond, is highly energetically unfavorable (>34 kcal/mol) ruling out attack at the C2 carbon on the $S = 1$ surface. Electrophilic attack on the C3 carbon of acac occurs on the $S = 2$ surface (Figure 16, structure 3b). Interaction of the superoxide (structure 2) with the acac HOMO leads to a two electron oxidation of the ligand HOMO to generate an Fe^{II}—peroxy bridged species. While the barriers to form a peroxy bridge to either C2 or C3 are very similar, as the calculated C3 bridged intermediate is a ferrous—peroxy species, the Fe^{II} can reductively cleave the O—O bond with a small (~2.2 kcal/mol) barrier. The distal oxygen transfers to the acac ligand and forms an epoxide, while the proximal oxygen is bound as an Fe^{IV}—oxo species (Figure 16 and Figure 17, structure 4b). To complete the reaction, the epoxide would open to form an ester (Figure 17, structure 5). The oxo would then attack the resultant C═C bond, transferring as an O atom and completing the reaction (Figure 17, structure 6 and Scheme 5).

Previous kinetics studies of the Dke1—acac/O_2 reaction found a number of important results. Briefly, $^{18}O_2$ labeling experiments found retention of the label in the acetate product and some exchange of the label in methyl glyoxal (70% retention

Scheme 5. Metal-Mediated O−O Cleavage in Dke1−acac

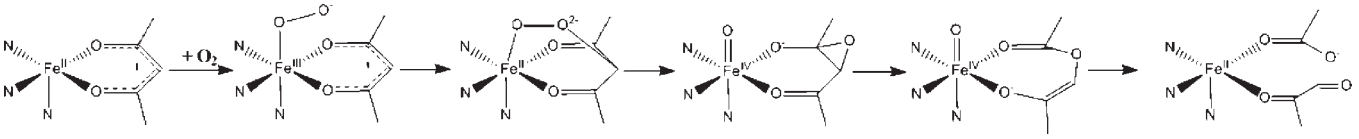

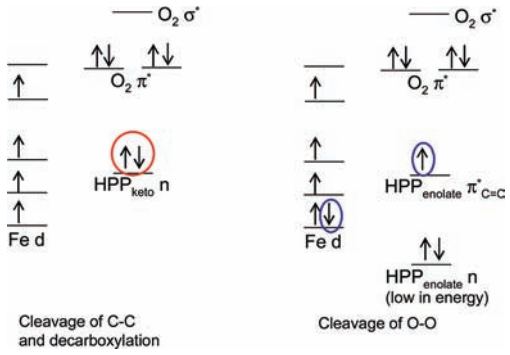

Figure 18. Comparison of electronic structures of peroxy bridged α-keto acid in HPP(keto) facial triad (left) and HPP(enolate) 3His triad (right). C−C cleavage in HPP(keto) occurs with transfer of an electron pair from the HPP(keto) n orbital to Fe (and subsequent transfer of an electron pair from Fe to the peroxide σ^* to cleave O−O) (ref 43). For the HPP(enolate) peroxy-bridge species, one electron from Fe and one from the HPP(enolate) $\pi^*_{C=C}$ are transferred directly to the peroxide σ^* to cleave the O−O bond.

of the label).[42] The rate of the reaction correlates with the energy of the HOMO of the substrate, and the rate-determining step is O_2-dependent and proposed to be associated with peroxide formation.[41] The computational mechanism presented above (Figure 16, top of Figure 17) is consistent with these results. The highest energy barrier in the reaction is the formation of the peroxy bridge between Fe and acac. The calculated free energy of activation in going from 1 to TS1 is 17 kcal/mol, while the experimental value (based on a rate of 6.6 s^{-1}) is 15 kcal/mol. The results in Figure 16 are also consistent with the lack of an observable Fe−O_2 species, as O_2 binding is significantly endergonic. Furthermore, the attack at C3 (Figure 16, 2 → 3b) is an electrophilic attack on the HOMO of the substrate, which could be dependent on the HOMO energy. Finally, in this mechanism, the distal O of O_2 is incorporated into the acetate product and would retain the label, whereas the Fe^{IV}=O could scramble with solvent, consistent with the partial label in the methyl glyoxal product (Scheme 5).

5. DISCUSSION

The O_2-dependent cleavage of HPP catalyzed by Dke1 yields products that are not observed in the reactions of the α-keto acid-dependent mononuclear nonheme iron enzymes that have facial triads with 2His/1 carboxylate ligation (Scheme 2). This standard α-keto acid reactivity involves decarboxylation of the acid (C1−C2 cleavage), while the products observed for the O_2-dependent cleavage of HPP by Dke1 indicate C2−C3 cleavage. Spectroscopic characterization of the Dke1−HPP complex, however, revealed a new enolate dianion binding mode for the α-keto acid. This is derived from the intense CT absorption signal and weak MCD features in Dke1−HPP relative to HPPD−HPP, the C=C rather than C=O stretch observed in the rR spectrum, and their corresponding computational modeling.

The assignment of HPP as an enolate bound to Dke1 and the associated spectral change from an MLCT transition (observed in the typical keto-bound α-keto acid dependent nonheme iron enzymes) to LMCT transitions (observed for the enolate-bound form in Dke1) reflect a difference in mechanistic pathways in the O_2 reactivity between the keto and enolate forms. The low-lying, unoccupied α-keto acid π^* orbital in the keto form allows for an interaction between the Fe−peroxy species and the α-keto acid LUMO (Figure 8, left). For the enolate form, the high-lying, occupied HPP(enolate) $\pi^*_{C=C}$ orbital allows the interaction between the Fe^{III}−superoxy species and the enolate HOMO (Figure 8, right). Attack on the HOMO versus LUMO of the respective substrates leads to Fe−peroxy bridged species with different electronic structures. In the α-keto acid reactivity of the facial triad containing α-keto acid dependent dioxygenases, the bridged Fe−α-keto acid−O_2 adduct has been calculated to be an Fe^{IV}−peroxide species.[43] For the enolate, the peroxy bridged species is an Fe^{III}−$HPP^{\bullet}$−O_2^{2-}. This difference in electronic structures then leads to the different reactivities observed experimentally. For the enolate bridged peroxy species, a lower barrier was found for O−O bond cleavage as compared to C−C bond cleavage; the latter would release CO_2 as is observed for the α-keto acid-dependent facial triad enzymes. Cleavage of the O−O bond requires two electron transfer into the peroxide σ^* orbital. For the Fe^{IV}−peroxide species in the keto form, the Fe site is fully oxidized; therefore, the electrons for cleavage of the O−O bond must come from the high lying, occupied α-keto acid n orbital. As this n orbital (HOMO in Figure 8, left) is primarily a lone pair on the carboxylate of the α-keto acid with some density along the C−C bond, transfer of the n electron pair breaks the C−C bond giving off CO_2 (Figure 18, left, red circle). For the enolized α-keto acid, which has a calculated Fe^{III}−$HPP^{\bullet}$−O_2^{2-} electronic structure, the equivalent of the n orbital is now low in energy and relatively unavailable for transfer to peroxide σ^*. Instead, the α radical on C3 of HPP(enolate) and the occupied β Fe d orbital are the α and β HOMOs, respectively (blue circles in Figure 18, right). Transfer of this electron pair to the peroxide σ^* results in cleavage of the O−O bond and formation of the Fe^{IV}−epoxide species. After formation of the Fe^{IV}−epoxide species, a low energy pathway was found to cleave the C2−C3 bond and release the products, oxalate and *p*-hydroxybenzaldehyde.

In both the enolate−O_2 reaction and the native Dke1−acac−O_2 reaction, a mechanism in which O_2 directly attacks the substrate HOMO has been proposed.[32,41] This approach was evaluated for the reaction of O_2 with the substrate for both the Dke1−HPP(enolate) and Dke1−acac complexes. For both complexes, the barrier to form the substrate-bound species is prohibitively high (>30 kcal/mol) and thus not likely mechanistically relevant. An examination of the transition state for these reactions shows that at the transition state, one electron has been

transferred to O_2 before significant formation of the O−C bond (O−C = ∼1.8 Å and the C shows little conversion to the sp^3 geometry, Supporting Information Figure S6). Thus, this corresponds to an outer sphere 1 e^- reduction of O_2 to superoxide by the substrate HOMO, which is not energetically favorable. This is in contrast to the transition state for the metal-mediated peroxy bridged species where binding to the Fe facilitates the inner sphere transfer of the first electron from the Fe to O_2.

The calculated mechanism of the O_2 reaction with acac in Dke1 parallels that for the atypical cleavage of HPP in Dke1. For both of these reactions, substrate binding opens a coordination position, thus enabling O_2 coordination to form a $Fe^{III}-O_2^{\bullet-}$ species. This species then reacts with the substrate HOMO to form a peroxy bridged species (either $Fe^{III}-HPP^{\bullet}-O_2^{2}$ or $Fe^{II}-O_2^{2-}$ with acac). Electron transfer from the Fe^{II} (or $Fe^{III}/HPP^{\bullet}$) into the peroxide σ^* orbital results in the reductive cleavage of the O−O bond to go to an Fe^{IV}−oxo species. In this way, the electron-donating properties of the Fe center with the bound anionic substrate facilitate formation of the peroxy species important in the cleavage of β-diketones.

In past studies, it was emphasized that the 2His/1 carboxylate facial triad played a role in binding the Fe^{II} to the protein with exchangeable coordination positions[5] and that the noncoordinated O of the carboxylate could H-bond to H_2O to keep the 6C bound form of the Fe^{II} when α-keto acid is bound in the absence of substrate.[44] Here, we have defined a difference in the nature of α-keto acid HPP binding to the facial versus 3His triads that demonstrates an important additional role for the facial triad in α-keto acid-dependent mononuclear nonheme iron enzymes. Analysis of the energies of the calculated structures of the keto and enol forms of HPP shows that the pK_a of the enol proton of HPP decreases by ∼10 log units going from coordination to a facial triad to coordination to a 3His triad. Thus, the negatively charged carboxylate of the facial triad stabilizes the monoanionic, keto structure of the bound α-keto acid, which allows this cofactor to provide the 2 e^-'s required for O−O bond cleavage and the generation of an Fe^{IV}=O species through decarboxylation (Figure 18, left).

■ ASSOCIATED CONTENT

Supporting Information. Full ref 18; key geometric parameters for HPP(keto) and HPP(enolate); pseudo-A intensity mechanism for LMCT; energy level diagrams for Dke1−HPP(enolate)−O_2 reaction; geometry-optimized structure of HPP(enolate) ester−Fe^{III}−oxo; transition state for substrate attack; and Cartesian coordinates for stationary structures. This material is available free of charge via the Internet at http://pubs.acs.org.

■ AUTHOR INFORMATION

Corresponding Author
edward.solomon@stanford.edu

■ ACKNOWLEDGMENT

This research was supported by NIH Grant GM40392 (E.I.S.) and the FWF (Austrian Science Fund) project P18828 (G.D.S.).

■ REFERENCES

(1) Solomon, E. I.; Brunold, T. C.; Davis, M. I.; Kemsley, J. N.; Lee, S. K.; Lehnert, N.; Neese, F.; Skulan, A. J.; Yang, Y. S.; Zhou, J. *Chem. Rev.* **2000**, *100*, 235–349.
(2) Neidig, M. L.; Solomon, E. I. *Chem. Commun.* **2005**, *47*, 5843–5863.
(3) Purpero, V.; Moran, G. R. *J. Biol. Inorg. Chem.* **2007**, *12*, 587–601.
(4) Hausinger, R. P. *Crit. Rev. Biochem. Mol. Biol.* **2004**, *39*, 21–68.
(5) Hegg, E. L.; Que, L. *Eur. J. Biochem.* **1997**, *250*, 625–629.
(6) Blasiak, L. C.; Vaillancourt, F. H.; Walsh, C. T.; Drennan, C. L. *Nature* **2006**, *440*, 368–371.
(7) Ueki, M.; Galonic, D. P.; Vaillancourt, F. H.; Garneau-Tsodikova, S.; Yeh, E.; Vosburg, D. A.; Schroeder, F. C.; Osada, H.; Walsh, C. T. *Chem. Biol.* **2006**, *13*, 1183–1191.
(8) McCoy, J. G.; Bailey, L. J.; Bitto, E.; Bingman, C. A.; Aceti, D. J.; Fox, B. G.; Phillips, G. N. *Proc. Natl. Acad. Sci. U.S.A.* **2006**, *103*, 3084–3089.
(9) Straganz, G. D.; Glieder, A.; Brecker, L.; Ribbons, D. W.; Steiner, W. *Biochem. J.* **2003**, *369*, 573–581.
(10) Straganz, G. D.; Diebold, A. R.; Egger, S.; Nidetzky, B.; Solomon, E. I. *Biochemistry* **2010**, *49*, 996–1004.
(11) Diebold, A. R.; Neidig, M. L.; Moran, G. R.; Straganz, G. D.; Solomon, E. I. *Biochemistry* **2010**, *49*, 6945–6952.
(12) For both HPPD and Dke1, there is no net charge from the second sphere residues, within 10 Å.
(13) Di Guiro, C. M. L.; Buongiorno, D.; Straganz, G. D. *J. Inorg. Biochem.* **2011**, *105*, 1204–1211.
(14) Straganz, G.; Brecker, L.; Weber, H. J.; Steiner, W.; Ribbons, D. W. *Biochem. Biophys. Res. Commun.* **2002**, *297*, 232–236.
(15) Pavel, E. G.; Kitajima, N.; Solomon, E. I. *J. Am. Chem. Soc.* **1998**, *120*, 3949–3962.
(16) Solomon, E. I.; Pavel, E. G.; Loeb, K. E.; Campochiaro, C. *Coord. Chem. Rev.* **1995**, *144*, 369–460.
(17) Frisch, M. J.; et al. *Gaussian 03*, revision E.01; Gaussian, Inc.: Pittsburgh, PA, 2007.
(18) Perdew, J. P. *Phys. Rev. B* **1986**, *33*, 8822–8824.
(19) Becke, A. D. *Phys. Rev. A* **1988**, *38*, 3098–3100.
(20) Schenk, G.; Pau, M. Y. M.; Solomon, E. I. *J. Am. Chem. Soc.* **2004**, *126*, 505–515.
(21) Cramer, C. J.; Truhlar, D. G. *Chem. Rev.* **1999**, *99*, 2161–2200.
(22) Dennington, R., II; Keith, T.; Millam, J.; Eppinnett, K.; Hovell, W. L.; Gilliland, R. *GaussView, Version 3.09*; Semichem, Inc.: Shawnee Mission, KS, 2003.
(23) Tenderholt, A. L. *QMForge, Version 2.1*.
(24) Schaftenaar, G.; Noordik, J. H. *J. Comput.-Aided Mol. Des.* **2000**, *14*, 123–134.
(25) Gorelsky, S. I. *SWizard program*, 2010.
(26) Gorelsky, S. I.; Lever, A. B. P. *J. Organomet. Chem.* **2001**, *635*, 187–196.
(27) Johnson-Winters, K.; Purpero, V. M.; Kavana, M.; Moran, G. R. *Biochemistry* **2005**, *44*, 7189–7199.
(28) The peak position of the 21 500 cm^{-1} band is shifted from the absorption intensity maximum due to the negative intensity in the MCD (seen at ∼25 000 cm^{-1}), which overlaps the high energy edge of the transition.
(29) Neidig, M. L.; Kavana, M.; Moran, G. R.; Solomon, E. I. *J. Am. Chem. Soc.* **2004**, *126*, 4486–4487.
(30) Attempts were made to excite into the 22 500 cm^{-1} band; however, no feature was observed above the intense fluorescence background.
(31) Ho, R. Y. N.; Mehn, M. P.; Hegg, E. L.; Liu, A.; Ryle, M. J.; Hausinger, R. P.; Que, L. *J. Am. Chem. Soc.* **2001**, *123*, 5022–5029.
(32) Paine, T. K.; England, J.; Que, L. *Chem.-Eur. J.* **2007**, *13*, 6073–6081.
(33) For these spin unrestricted, open shell systems, occupied orbitals are spin polarized to low energy and very mixed. For the bonding description generated here, we use the unoccupied antibonding orbitals to define the uncompensated occupied orbitals involved in bonding.
(34) The tautomers of the free HPP ligands are not directly compared because in free enolized HPP, the double bond between C2−C3 is delocalized across the entire ligand, while when bound to Fe,

the negative charge on the alkoxide oxygen is stabilized and the double bond is delocalized on C2−C3.

(35) Neidig, M. L.; Brown, C. D.; Kavana, M.; Choroba, O. W.; Spencer, J. B.; Moran, G. R.; Solomon, E. I. *J. Inorg. Biochem.* **2006**, *100*, 2108–2116.

(36) Another substrate (2-oxo-4-phenylbutanoate) in which the C−C double bond cannot conjugate with the phenyl ring was also evaluated. The enolized form is not observed in the absorption spectrum, and the reaction with O_2 yields only the decarboxylated product. See Supporting Information Figure S2 for further details.

(37) Solomon, E. I.; Hanson, M. A. Bioinorganic Spectroscopy. In *Inorganic Electronic Structure and Spectroscopy*; Solomon, E. I., Lever, A. P. B., Eds.; Wiley: New York, 1999; Vol. II.

(38) Using the vibrations predicted by the calculations, the C═O stretch of α-keto acid bound to a facial triad is 1698 cm^{-1}, in good agreement with the experimentally observed value of 1686 cm^{-1}, indicating that these computational models predict vibrational data that are comparable with the experimental data.

(39) As the ferrous center has $S = 2$ and O_2 has $S = 1$, the $S = 1$, $S = 2$, and $S = 3$ total spin states were considered for the substrate attack.

(40) The distance between Fe and C3 (∼3.7 Å) is too far for O_2 to bridge.

(41) Straganz, G. D.; Nidetzky, B. *J. Am. Chem. Soc.* **2005**, *127*, 12306–12314.

(42) Straganz, G. D.; Hofer, H.; Steiner, W.; Nidetzky, B. *J. Am. Chem. Soc.* **2004**, *126*, 12202–12203.

(43) Diebold, A. R.; Brown-Marshall, C. D.; Neidig, M. L.; Brownlee, J. M.; Moran, G. R.; Solomon, E. I., submitted.

(44) Neidig, M. L.; Brown, C. D.; Light, K. M.; Fujimori, D. G.; Nolan, E. M.; Price, J. C.; Barr, E. W.; Bollinger, J. M.; Krebs, C.; Walsh, C. T.; Solomon, E. I. *J. Am. Chem. Soc.* **2007**, *129*, 14224–14231.